Methods

1. Experimental

Reconstruction of the populations in the regular islands - Due to sub-wavelength spacing between the regular islands, we cannot measure in-situ by optical means the atomic populations in each island. To circumvent this limitation, we use two experimental tricks: (i) we perform a $\pi/2$ phase space rotation: by letting the system evolve for an additional $T/2$ time in the modulated lattice, the atomic wavepacket initially on the right (resp. left) island acquires a negative (resp. positive) momentum (see SI); (ii) we subsequently switch off all trapping potentials and perform a 25 ms time-of-flight before taking an absorption image.

The corresponding patterns (see both Fig. 1**e** of the main text and Fig. 1**a-d** of Methods) consist in regularly spaced interference peaks centered about discrete momenta $p_j = jh/d$, with j an integer and d the lattice spacing. We identify the zero-momentum peak position by a preliminary experiment performed on a static lattice. We then label each peak with its corresponding discrete momentum value. The population initially in the right (resp. left) island is then determined from the integration of the peaks with negative (resp. positive) momenta after the time-of-flight. Performing the experiment for different times in the modulated lattice (an even number of modulation periods $n \times 2T$), we infer the time evolution of the populations (see Fig. 1**i** of Methods).

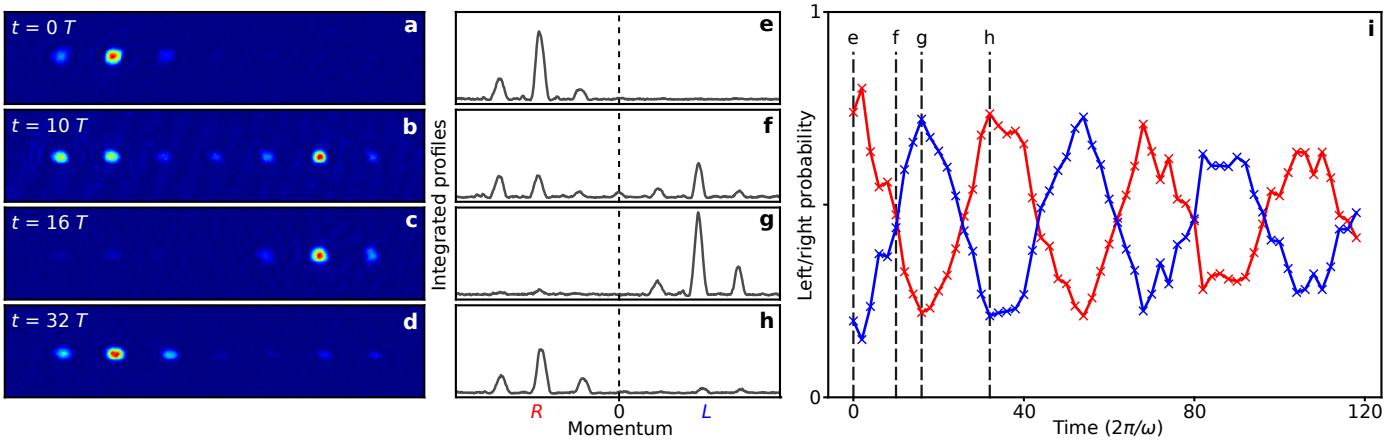

Fig. 1 | Determination of the populations in the left and right islands. a-d, Experimental absorption images taken after a 25 ms time-of-flight for different numbers of modulation period. **e-h**, Solid lines: profiles of the experimental images integrated along the vertical axis, giving access to the momentum distribution along the lattice axis (the dashed line separates the positive and negative momentum components). **i**, Time-evolution of the population of the right (red color) (resp. left (blue color)) regular island obtained from the integration of the momentum profiles (e.g. **e-h**) over negative (resp. positive) momenta.

Bifurcation - For a given phase space (see Fig. 2**a-c** of Methods), we can probe experimentally the number and position(s) of the regular island(s) along the x-axis. For this purpose, we load the lattice adiabatically and then shift suddenly the lattice by a distance Δx before modulating the lattice amplitude for a few modulation periods (an even number of periods between 4 to 10). This choice of modulation time results from a trade-off: the tunneling is still marginal while the spreading of the wave packet when placed in the chaotic zone is clearly visible. The analysis is performed after a 25 ms time-of-flight absorption image which reveals the momentum distribution. The dispersion in momentum is extracted from the integrated profile of the experimental images (see e.g. Fig. 1**e-h** of Methods). Using a multi-Gaussian fit of this momentum dispersion plotted as a function of the initial offset Δx (see Fig. 2**d-f** of Methods), we extract the position(s) for which the momentum dispersion is minimal, and therefore infer the position(s) of the center(s) of the regular island(s).

Oscillation frequency extraction - To extract experimental oscillation frequencies (see Figs. 4 of the main text, 4**c** and 5**c** of SI), we compute the Fourier spectra of the time evolution of the left and right populations. We extract from their average a main peak and keep the secondary peaks only when their weight is at least $1/3$ of the main one, a choice that captures efficiently the main characteristics of the oscillations. Each

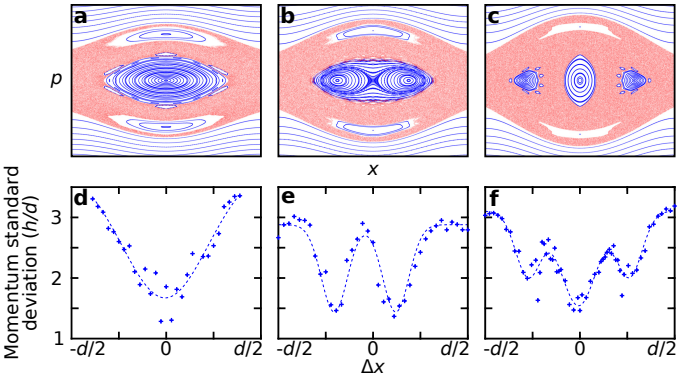

Fig. 2 | Determination of regular island(s) position(s). Phase space generated by the parameters $\epsilon = 0.268$ and **a** $\gamma = 0.188$, **b** $\gamma = 0.265$, **c** $\gamma = 0.348$, showing the splitting of the central regular island into two and three islands. **d-f**, Experimental results associated to each phase space: the standard deviation of the atomic momentum distribution is plotted as a function of the in-trap initial position Δx of the atomic wave packet. Dotted lines: multi-Gaussian fits.

frequency is determined from a three-point average around the corresponding maximum. The error on the frequency determination is assumed to follow a triangular law around the maxima with an uncertainty of $\pm f_0/(2\sqrt{6})$, where f_0 is

the sampling rate.

2. Numerical

The numerical simulations compute the evolution of an interaction-free wavefunction in the time-dependent potential using the split-step method. For Figs. 4**a** and **b** of the main text, and 4**c** and 5**c** of the SI, the dynamics is simulated on a single cell of size equal to the lattice spacing.

The mixed classical phase space exhibits two stable islands symmetric in position. The initial state is a Gaussian wave packet placed at the center of one of the islands with the following relations between the quadratic sizes in position and momentum $\Delta x = 2\Delta p$ to maximize the overlap with the classical lateral island. The observable probed every two periods is the modulus squared of the overlap either with the initial state or its symmetrical partner centered on the other island. The oscillation frequencies are obtained from the Fourier transform performed over 10,000 periods.

In the more realistic simulations of Figs. 4**d**-**f** of the main text, we consider a system made of 151 cells and we initially populate the same island on 13 successive cells.

The analysis in terms of Floquet eigenstates, relevant for Fig. 3 of the main text, is inferred from the evolution operator (Floquet operator) over two periods. Quasi-energies are directly extracted from the phase of the eigenvalues.

Supplementary Information

1. Bifurcation and rotation in phase space

The bifurcation - To introduce the main features of the bifurcation, we linearize the classical equation of motion close to $x = 0$ and introduce explicitly the period of modulation T. In this way, we get at third order of expansion the Mathieu-Duffing equation:

$$\frac{\mathrm{d}p}{\mathrm{d}t} + \gamma\left(1 + \varepsilon\cos\left(2\pi\frac{t}{T}\right)\right)\left(x - \frac{x^3}{6}\right) = 0. \tag{1}$$

The standard linear Mathieu equation displays instabilities (unbounded solutions) for a discrete set of ratios between the forcing and the natural frequencies ($\propto \sqrt{\gamma}$). The non-linearities of Eq. (1) shifts those resonances and can even restore their stability. This latter effect is responsible for the bifurcation.

According to the analytical approach developed in Refs. [1, 2], the bifurcations occur at two critical values $\gamma_c = (1 \pm \varepsilon/2)^{-1}$. For a fixed amplitude of modulation, ε, the first bifurcation when the lattice depth γ is increased amounts to breaking the central stable island into two off-centered symmetric stable islands whose phase space coordinates are given by

$$\begin{pmatrix} x^\star \\ p^\star \end{pmatrix} = \pm\sqrt{8\left(1 + \frac{\varepsilon}{2} - \frac{1}{4\gamma}\right)}\begin{pmatrix} \cos(\pi t/T) \\ \sin(\pi t/T)/2 \end{pmatrix}. \tag{2}$$

For our parameter ($\varepsilon = 0.268$), this bifurcation occurs at $\gamma = 0.22$. In the range $0.22 < \gamma < 0.29$, the $(x, p) = (0, 0)$ orbit becomes unstable. For $\gamma > 0.29$, the stability of this orbit is restored (see Fig. 2 of the main text).

Rotation in phase space and $2T$ formalism - Equation (2) actually describes the forced motion of a pair of stable points in the (x, p) plane. They rotate with a $2T$ period on an ellipse centered on $(x, p) = (0, 0)$ (see Fig. 3 of SI). This is the reason why (i) we probe the system stroboscopically every $2T$ and (ii) we wait for an extra $T/2$ period to transfer the information from the x-axis to the p-axis.

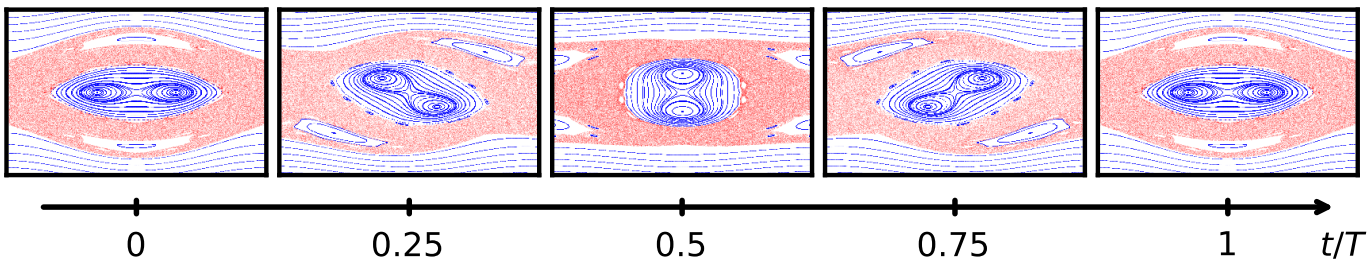

Fig. 3 | Rotation of the stable orbits in phase space. Stroboscopic phase spaces are plotted for different values of the modulation time showing the rotation of the two symmetric islands. Parameters: $\epsilon = 0.15$, $\gamma = 0.25$.

2. Additional experimental CAT resonances

CAT resonances are a very generic feature of mixed systems. We report hereafter two other observations performed with different parameters showing three additional resonances (see Figs. 4 and 5 of SI). The experimental data are in very good agreement with the numerical simulations.

3. Spectrum and eigenstates analysis of the experimental CAT resonances

The theoretical description of chaos-assisted tunneling resonances involves an avoided crossing scenario between regular and chaotic states. This description rests on the semi-classical approximation ($\hbar_{\mathrm{eff}}$ small enough compared to the size of the classical structures of the phase space) that guarantees to be able to label chaotic and regular states. For

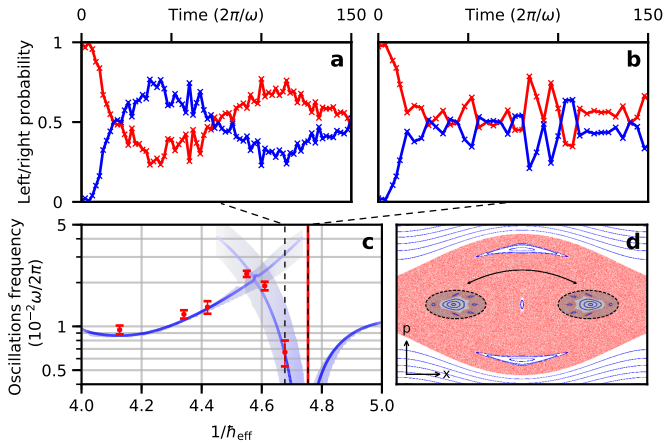

Fig. 4 | Second experimental CAT resonance. **a-b**, Examples of experimental tunneling oscillations. **c**, Experimentally measured tunneling frequencies (red dots) as a function of $\hbar_{\rm eff}^{-1}$ compared to the theoretical/numerical predictions corresponding to $\gamma = 0.315 \pm 0.005$ and $\varepsilon = 0.39$. The vertical red line indicates a dataset right at resonance for which we couldn't extract a frequency. The blue shaded area corresponds to the experimental uncertainty on γ. The corresponding classical phase space is plotted in (**d**).

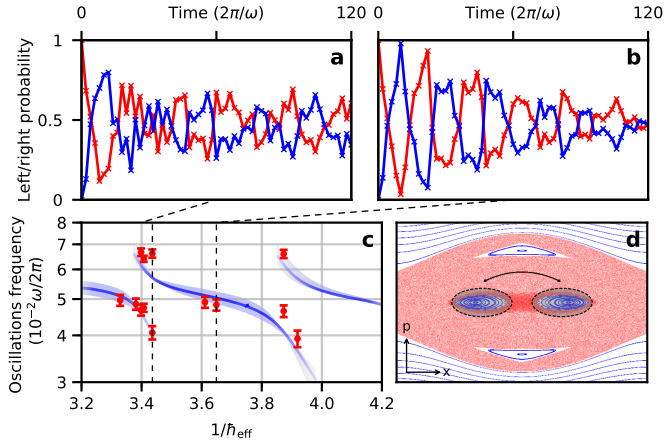

Fig. 5 | Third and fourth experimental CAT resonances. **a-b**, Examples of experimental tunneling oscillations. **c**, Experimentally measured tunneling frequencies (red dots) as a function of $\hbar_{\rm eff}^{-1}$ compared to the theoretical/numerical predictions corresponding to $\gamma = 0.229 \pm 0.001$ and $\varepsilon = 0.60$. The blue shaded area corresponds to the experimental uncertainty on γ. The corresponding classical phase space is plotted in (**d**).

the three experimental configurations we probed, the quasi-energy spectra show avoided crossings associated with the observed resonances (see Figs. 6**a**, 7**a**, 8**a** of SI) and the states involved can be labelled in two classes: regular (see Figs. 6**b-c**, 7**b-c**, 8**b-c** of SI) and chaotic (see Figs. 6**d-e**, 7**d-e**, 8**d-e** of SI).

4. Oscillation damping

As stated in the main article, the number of atoms in the condensate drastically affects the damping of the chaos-assisted tunneling oscillations (see Fig. 9 of SI). We attribute this effect to the dephasing of BECs in each lattice site due to interatomic interactions. As the strength of the interaction depends on the density, reducing the number of atoms decreases the damping rate.

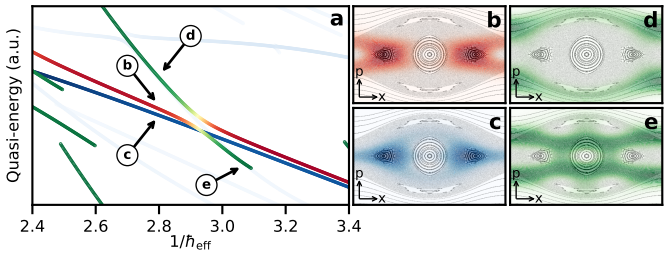

Fig. 6 | Eigenstates analysis of the first experimental CAT resonance (see Fig. 4 of main text). **a**, quasi-energy spectrum of the quantum states involved in the CAT resonance. To identify the relevant eigenstates, we compute their overlap with a Gaussian state placed at the center of one of the lateral islands. In blue: regular eigenstate having a given parity. In red: regular eigenstate with the opposite parity. In green: chaotic states. Red (regular state) to green (chaotic state) curves reveal the mixing between regular and chaotic states having the same parity (avoided crossing). (**b, c, d, e**) Husimis distribution of the relevant eigenstates superimposed to the classical phase space.

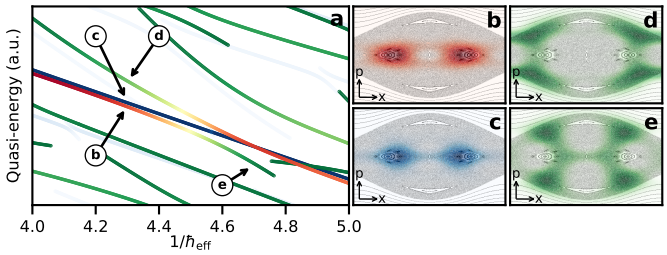

Fig. 7 | Eigenstates analysis of second experimental CAT resonance (see Fig. 4 of SI). Same convention as Fig. 6.

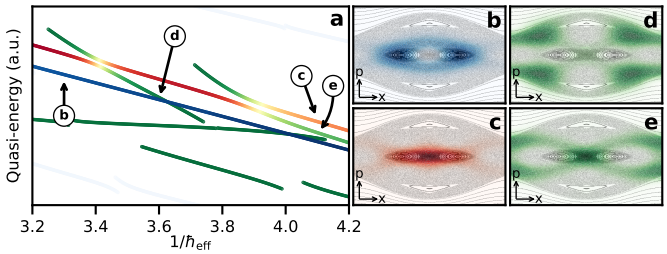

Fig. 8 | Eigenstates analysis of the third and fourth experimental CAT resonances (see Fig. 5 of SI). Same convention as Fig. 6.

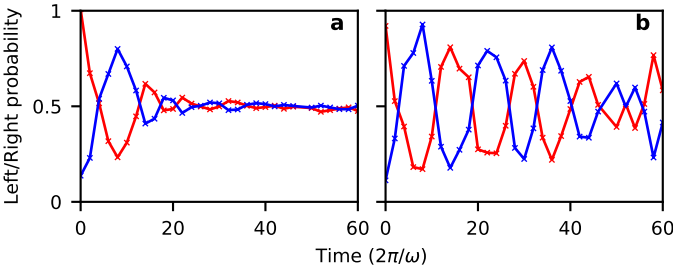

Fig. 9 | Damping of oscillations with the number of atoms. Comparison of the chaos-assisted tunneling oscillations for two different atom numbers: **a** $N = 1.2 \pm 0.2 \times 10^5$ and **b** $N = 4 \pm 0.2 \times 10^4$. The phase space parameters are $\gamma = 0.225 \pm 0.005$ and $\varepsilon = 0.59 \pm 0.01$.

[1] A. Mouchet and D. Delande, Phys. Rev. E **67**, 046216 (2003).
[2] Kovacic, I., Rand, R., and Mohamed Sah, S., Appl. Mech. Rev. **70**, 020802 (2018).